ACS APPLIED ENERGY MATERIALS

www.acsaem.org Article

Organocatalysis-Inspired Palladium Molecule as a Robust Polysulfide-Confinement-Scissors Catalyst for Advanced Lithium–Sulfur Battery

Binbin Gu, Shuo Yang,* Dong Cai, Yangyang Dong, Shuang Yu, Tingting Li, Huagui Nie, and Zhi Yang*

Cite This: *ACS Appl. Energy Mater.* 2022, 5, 8538–8546 Read Online

ACCESS | Metrics & More | Article Recommendations | Supporting Information

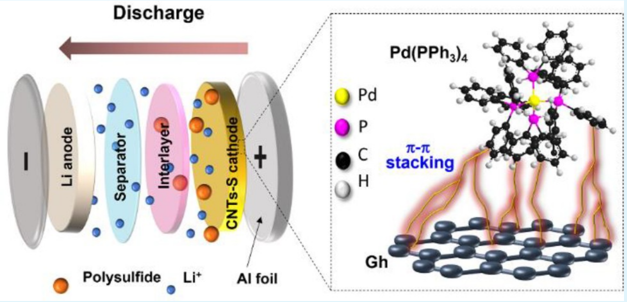

ABSTRACT: The rational design of effective polysulfide catalysts to alleviate shuttle effects and improve sulfur conversion kinetics is still a significant challenge for high-performance lithium−sulfur batteries. The organometallic palladium molecule comes to mind because of its ultrahigh catalytic activity in many industrial syntheses. Herein, a tetrakis(triphenylphosphine)palladium (TPP) catalyst decorated graphene (Gh) interlayer sandwiched between the sulfur infiltrated carbon nanotubes' (CNTs-S) cathode and the separator is developed. A combination of in situ spectroscopy, electrochemical characterization, and theoretical calculations unveils that in the battery system, the dissociation of a triphenylphosphine (PPh_3) opens the lid of TPP and thus provides enough space for absorbing/catalyzing both long-chain and short-chain lithium polysulfides (LiPSs) via Pd−S bonds, while a great number of P atoms in TPP with good Li^+ affinity can homogenize the Li^+ flux and facilitate Li^+ transport in the battery through P−Li bonds. Because of the synergistic effect, lithium−sulfur batteries using a CNTs-S/Gh/TPP cathode manifest an excellent cycle stability with a high capacity retention of 83.7% and an areal capacity of 2.44 mAh cm^{-2} during 180 cycles at 0.1 C under a high sulfur loading of 4.43 mg cm^{-2}. This work builds a bridge between organic catalysis and an electrochemical battery.

KEYWORDS: *lithium−sulfur batteries, lithium polysulfides, catalysts, tetrakis(triphenylphosphine)palladium, interlayers*

■ INTRODUCTION

With the urgent desire for high-energy-density rechargeable devices, a lithium−sulfur (Li−S) battery is deemed as the most attractive energy storage device beyond transitional Li-ion batteries because of its low cost and drastically superior specific energy.[1] However, the principal problems of Li−S battery are the sharp capacity degradation and poor cycle life caused by the migration of intermediate lithium polysulfides (LiPSs) and the sluggish reaction kinetics of complex transformation process, which is a formidable challenge facing the commercialization of Li−S batteries.[2] Fortunately, considerable studies have been performed to solve these problems by cathode modification, including employing nonpolar porous carbon hosts[3−6] or interlayers[7] to physically entrap LiPSs and restrict their movement and developing effective polar adsorbents (e.g., functionalized carbon,[8] metal oxides,[9−11] metal organic frameworks,[12] and MXenes[13]) to chemically anchor LiPSs at the cathode side. Despite some positive effects to suppress the shuttle effect, the slow LiPS conversion kinetics problem is hard to be solved fundamentally just through such physical and chemical confinement strategies.

To overcome the shuttle effect and improve the reaction kinetics of LiPSs simultaneously, a wide variety of catalysts (e.g., metals,[14] metal sulfides,[15] and metal phosphides[16,17]) have been adopted. Although there have been advances in enhancing the battery performance, the poor electronic conductivity and low active site utilization of the solid catalysts usually cannot meet the requirements for adsorption of a large amount of LiPSs. Thus, rational exploration of more efficient catalysts for LiPS conversion is still a great challenge.

Palladium (Pd)-based molecular catalysts, which have a high tolerance for various functional groups, have been considered as an omnipotent solution to catalyze many important reactions in organic synthesis, pharmaceutical chemistry, and material science fields (as shown in Figure S1).[18,19] In view of the dominant position of Pd-based molecular catalyst in catalytic industry, introducing it into battery systems to catalyze electrochemical surface reactions seems a good strategy for improving the battery performance. Very recently, a clue can be found in the fuel cell field. An outstanding oxygen

Received: April 11, 2022
Accepted: June 21, 2022
Published: July 4, 2022

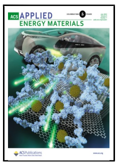

https://doi.org/10.1021/acsaem.2c01078

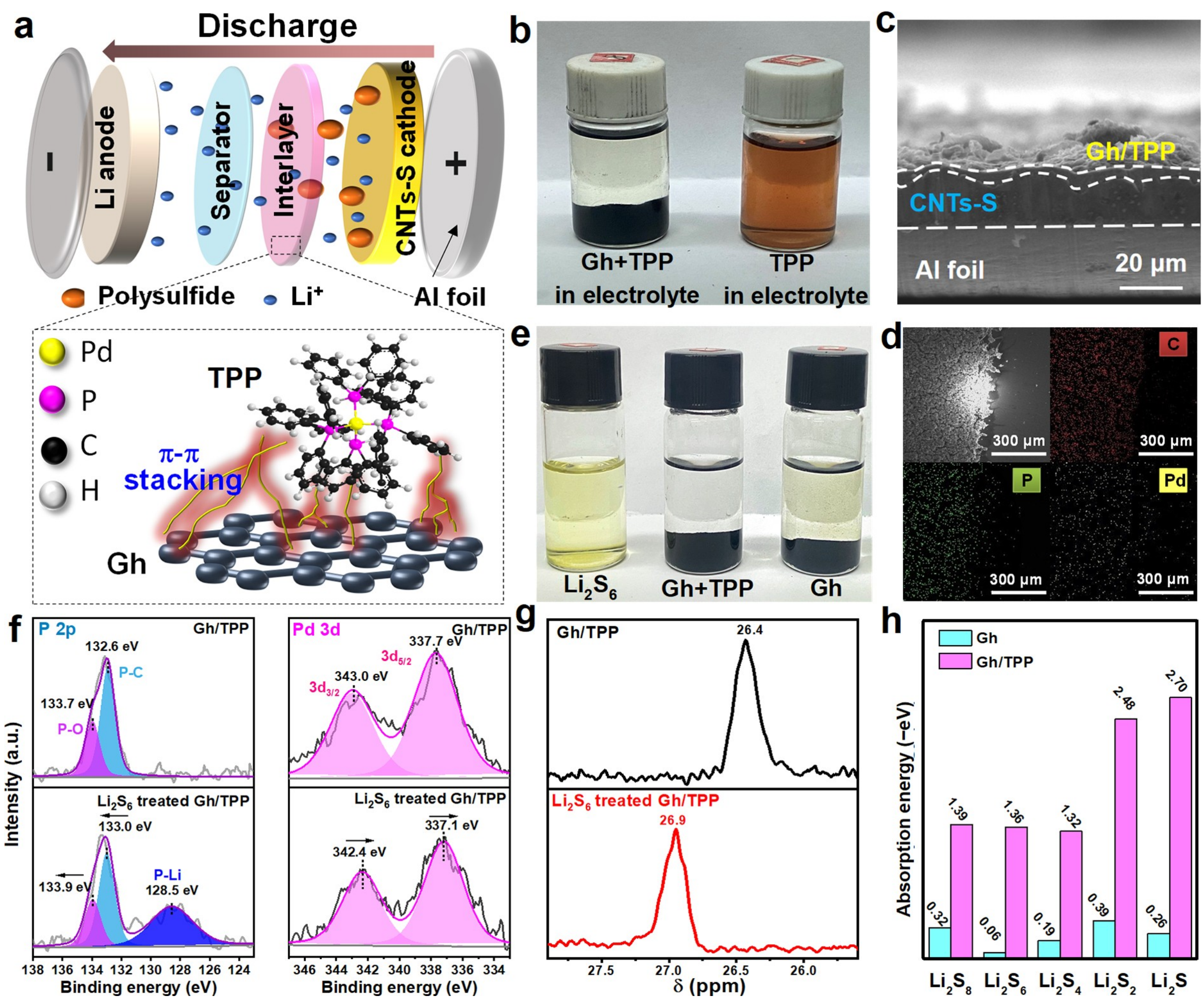

Figure 1. (a) Schematic illustration of Li−S batteries with Gh/TPP interlayer. (b) Optical photographs of TPP and Gh/TPP in electrolytes. (c) The cross-sectional SEM image of CNTs-S cathode with Gh/TPP interlayer. (d) EDX mapping images of C, P, and Pd elements corresponding to the top-view SEM image the of CNTs-S/Gh/TPP composite cathode. (e) Optical photographs of pristine Li_2S_6 electrolyte, Gh/TPP, and Gh soaked in the Li_2S_6 solution after 6 h. (f) High-resolution XPS spectra of P 2p and Pd 3d for Gh/TPP without and with Li_2S_6 adsorption. (g) ^{31}P NMR spectra of Gh/TPP and Li_2S_6-treated Gh/TPP. (h) The E_{ads} between Li_2S_n (n = 8, 6, 4, 2, 1) and Gh and Gh/TPP ($Pd(PPh_3)_x$, x = 3).

reduction reaction (ORR) kinetics was achieved at a Ni−N_4 site.[20] In the element periodic table, sulfur is in the next period of oxygen, and the elements in the next period of Ni and N are Pd and P, respectively. Motivated by our recent work on periodic expansion catalysis,[21] a material with a Pd−P_4 site should be promising for catalyzing sulfur reduction reaction (SRR) kinetics. On the basis of this background, tetrakis(triphenylphosphine)palladium (TPP, $Pd(PPh_3)_x$, x = 4) comes to mind because of its low cost, wide universality to the substrate, and ultrahigh catalytic efficiency in coupling reactions, as illustrated by the Nobel Prize in 2010. Therefore, in this contribution, we present a Li−S battery with good cycle life and electrochemical performance by using TPP supported on a graphene (Gh) interlayer connected to the sulfur infiltrated carbon nanotubes' (CNTs-S) cathode current collector (as schematically shown in Figure 1a). A combination of in situ spectroscopy, theoretical simulations, and electrochemical techniques was used to comprehensively clarify the interfacial reaction mechanisms. As far as we know, this is the first utilization of TPP as a catalyst in Li−S chemistry, which successfully builds a bridge between organic catalysis and electrochemical battery.

RESULTS AND DISCUSSION

Material Structures. The structural characteristics of Gh/TPP were first investigated by X-ray photoelectron spectroscopy (XPS). As found in Figure S2, after combining with Gh, the Pd 3d and P 2p XPS peaks of TPP shift to higher binding energy regions, indicating TPP combines with Gh via a strong $\pi-\pi$ stacking interaction.[22] The successful combination of TPP with Gh was also confirmed by Fourier transform infrared (FTIR) study of Gh/TPP (Figure S3), in which the characteristic vibration bands of Gh at 1634.2 cm^{-1} and the TPP at 686.5, 1121, 1434, and 3051 cm^{-1} can be clearly distinguished. Thanks to the $\pi-\pi$ interaction, the Gh/TPP composites become insoluble in the electrolyte, which contrasts sharply with the high solubility of TPP in electrolyte (Figure 1b). Thereupon, the as-synthesized Gh/TPP composite was coated on a CNTs-S cathode as an interlayer via a simple scraping process (denoted as CNTs−S/Gh/TPP). For comparison, a reference Gh-modified CNTs−S cathode was also prepared (denoted as CNTs−S/Gh). Figure 1c gives a cross-section scanning electron microscopy (SEM) image of the CNTs-S cathode capped by the Gh/TPP interlayer, revealing an ultrathin Gh/TPP interlayer with a thickness of

https://doi.org/10.1021/acsaem.2c01078
ACS Appl. Energy Mater. 2022, 5, 8538−8546

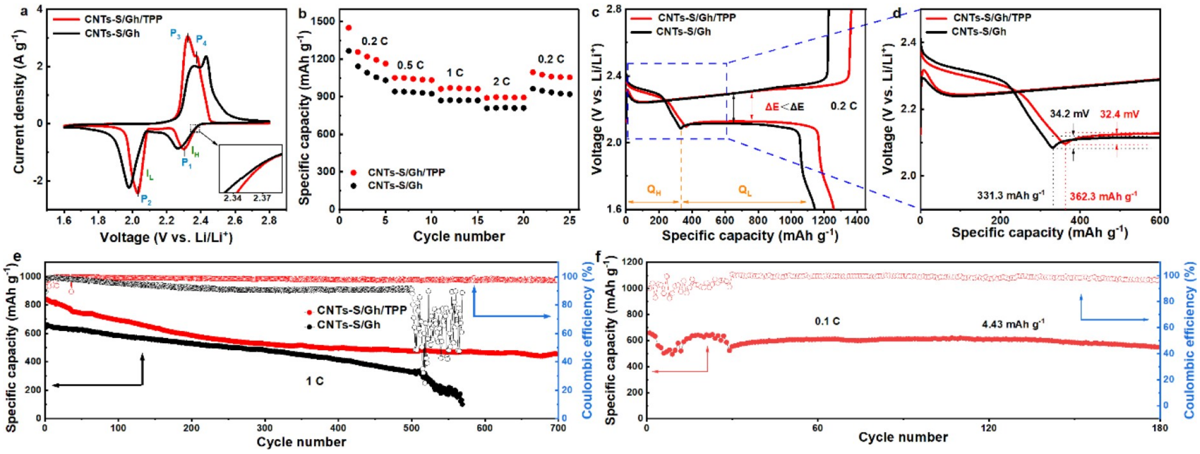

Figure 2. (a) The CVs of the CNTs−S/Gh/TPP and CNTs−S/Gh electrodes between 1.6 and 2.8 V for the second cycle (sweep rate: 0.1 mV s^{-1}). (b) Rate capabilities of the CNTs−S/Gh/TPP and CNTs−S/Gh electrodes cycled from 0.2 to 2 C. (c) The second galvanostatic charge/discharge voltage profiles of CNTs−S/Gh/TPP and CNTs−S/Gh-based batteries at 0.2 C. Q_H and Q_L are defined as the capacities at higher and lower discharge platforms, respectively. (d) The amplification of the charge/discharge profiles in Figure 2c. (e) Cycling performance with Coulombic efficiency of CNTs−S/Gh/TPP and CNTs−S/Gh electrodes assembled Li−S batteries at 1 C (sulfur loading = ∼ 1.5 mg cm^{-2}). (f) Cycling performance with Coulombic efficiency of CNTs−S/Gh/TPP electrode at 0.1 C (sulfur loading = ∼ 4.43 mg cm^{-2}).

∼4.0 μm contacts well with the CNTs-S (∼20.0 μm) cathode surface. Notably, the weight of the TPP accounts for only ∼1.3% of the whole composite cathode. The homogeneous distribution of TPP molecules in the interlayer was confirmed by the energy dispersive X-ray (EDX) mappings of CNTs-S/Gh/TPP composite cathode (Figure 1d), where P, Pd and C elements are uniformly distributed on the cathode surface.

Strong adsorption with LiPSs is the premise of the sulfur conversion process in a Li−S system; thus, a visual discrimination test for adsorption capability toward Li_2S_6 was carried out. Gh possesses a certain physical adsorption ability to Li_2S_6 due to its porosity, as probed by the Brunauer−Emmett−Teller (BET) results (Figure S4). Nevertheless, the physical adsorption strength of the host material is too limited to trap Li_2S_6 efficiently, resulting in a pale-yellow solution, as found in Figure 1e. In contrast to the Gh sample, Gh/TPP shows a strong fixation with LiPSs, which would be beneficial for the subsequent catalytic conversion of LiPSs. To understand the binding of Gh/TPP toward LiPSs, XPS measurements were performed before and after adsorption of Li_2S_6. As presented in Figure 1f, after fully interacting with Li_2S_6, obvious shifts to higher and lower binding energy for P 2p and Pd 3d peaks are observed on Gh/TPP, respectively. Moreover, a P−Li peak (128.5 eV) emerges in the P 2p spectrum of Li_2S_6 on Gh/TPP (Figure 1f).[23] These results verify the existence of chemical adsorption between soluble LiPSs and TPP via the transfer of electrons from P to Li. The ^{31}P NMR spectra of Gh/TPP with and without Li_2S_6 (Figure 1g) further demonstrate that the peak in Gh/TPP has an upshift of ∼0.5 ppm with the presence of Li_2S_6, indicating the P nucleus is more deshielded by Li_2S_6 environments, which in turn confirms the strong binding between P of TPP and Li of LiPSs. In addition, density functional theory (DFT) calculations were also conducted to evaluate the interaction strength between LiPSs and Gh/TPP surface. Before modeling the molecular configurations, the dissociation energies of TPP were first calculated on the basis of the fact that TPP undergoes a spontaneous dissociation of a PPh_3 in solution environment, releasing a $Pd(PPh_3)_3$ with 16 electrons to participate the reactions. As shown in Table S1, it takes the least energy for a TPP molecule to remove a PPh_3, and a further dissociation is thermodynamically unfavorable. Thus, the TPP ($Pd(PPh_3)_x$, $x = 3$) was used for following modeling. Figure S5 shows the side views of the optimized adsorption configurations for various LiPSs (Li_2S_n, n = 8, 6, 4, 2, 1) on Gh and Gh/TPP surfaces, where the LiPSs obtain more electrons from TPP via S−Pd bond. The calculated adsorption energies (E_{ads}) are given in Figure 1h. All these E_{ads} values of Li_2S_n + Gh/TPP (n = 8, 6, 4, 2, 1) are lower than those for Li_2S_n (n = 8, 6, 4, 2, 1) binding with Gh, which demonstrates that the cathode active materials are effectively anchored on Gh/TPP. The results are in agreement with the above adsorption and XPS experiments. Due to the synergistic effect of physical and chemical interaction with LiPSs, the yellow color of the Li_2S_6 solution fades and turns nearly colorless with the addition of Gh/TPP powder after 6 h (Figure 1e), although the specific surface area and mesopore volume of Gh/TPP are smaller than those of Gh (Figure S4), confirming the better Li_2S_6 adsorption capability of Gh/TPP than the pure Gh. The reason for the lack of Li_2S_6 adsorption test directly using pure TPP is the high solubility of TPP in 1,3-dioxolane (DOL)/1,2-dimethoxyethane (DME) solution, as shown in Figure S6.

Electrochemical Properties. To examine the superiority of TPP for enhancing the electrochemical properties of the cathode, cyclic voltammetry (CV), rate performance, galvanostatic charge/discharge profile, and cycling stability tests were carried out on the assembled Li−S batteries with CNTs−S/Gh/TPP electrodes. The TPP catalyst mass ratio to Gh of 1:5 in the interlayer is proved to be optimum for the battery performance (see Figure S7). The CV curves of the sulfur cathodes with and without TPP are shown in Figure S8. The cathodic sweep produces the two pronounced peaks at ∼2.3 (P_1) and ∼2.05 V (P_2), which stand for the transformation of S_8 to soluble LiPSs and subsequently to insoluble Li_2S_2/Li_2S, respectively, while the anodic scan presents two separated peaks at ∼2.3 (P_3) and 2.35 V (P_4), corresponding to the transformation from Li_2S_2/Li_2S to LiPSs and eventually S_8.[24−27] It is evident that the CNTs−S/Gh/TPP electrode is able to maintain an excellent cyclic reversibility based on well-overlapped CV curves after the first cycle (Figure S8).[28]

https://doi.org/10.1021/acsaem.2c01078
ACS Appl. Energy Mater. 2022, 5, 8538−8546

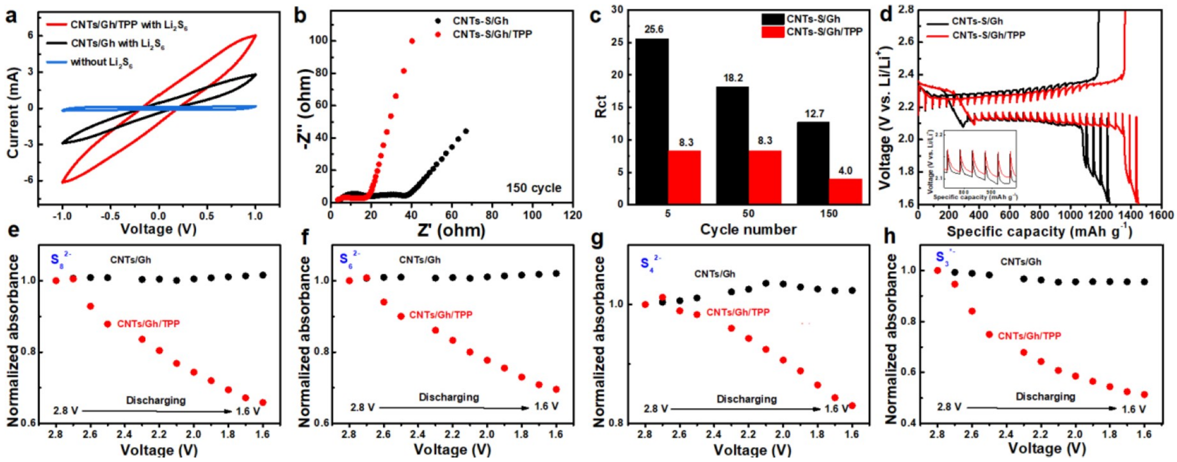

Figure 3. (a) CVs of Li_2S_6 symmetric cells between −1.0 and 1.0 V (scan rate: 0.1 mV s^{-1}). (b) The Nyquist plots of the two electrodes after 150 cycles. (c) The fitted R_{ct} values of CNTs-S/Gh/TPP and CNTs-S/Gh electrodes at different cycles. (d) GITT profiles of the two cathodes for the first discharge and charge. The potential-dependent normalized intensity of (e) $S_8{}^{2-}$, (f) $S_6{}^{2-}$, (g) $S_4{}^{2-}$, and (h) $S_3{}^{*-}$ at CNTs/Gh/TPP and CNTs/Gh electrode surfaces during discharge.

Furthermore, the second-cycle CVs of both cathodes are plotted in Figure 2a. In contrast to CNTs−S/Gh, the CNTs−S/Gh/TPP electrode exhibits a lower voltage hysteresis (ΔV, Table S2), a larger collection coefficient (I_L/I_H, Table S2), a higher reduction/oxidation current along with an obvious shift to positive/negative potential (Figure S9), and a smaller Tafel slope (Figure S10), suggesting the introduction of TPP into a cathode can efficiently improve redox reactivity and reduce the electrochemical polarization by kinetically accelerating the sulfur electrochemical reactions. Figure 2b shows the rate capabilities of the Li−S batteries assembled by CNTs−S/Gh/TPP and CNTs−S/Gh electrodes. The considerable discharge capacities of 1451.3, 1050.9, 963.1, and 890.9 mAh g^{-1} are obtained by CNTs−S/Gh/TPP-based battery at 0.2, 0.5, 1, and 2 C (1 C = 1675 mA g^{-1}), respectively; as the rate returns to 0.2 C, its discharge capacity is rapidly recuperative to 1096.7 mAh g^{-1}. The discharge capacities for the CNTs−S/Gh/TPP-based battery are 12% higher than those of the CNTs−S/Gh-based battery (1266.3, 941.8, 869.5, and 808.2 mAh g^{-1} at 0.2, 0.5, 1, and 2 C, respectively) at the same rate, illustrating the preponderant rate capacities and high electrochemical reversibility relating to the effective catalytic activity of TPP.

In the galvanostatic charge/discharge voltage profiles of the CNTs−S/Gh/TPP electrode (Figure 2c and Figure S11a), two long and flat discharge/charge voltage plateaus, a small voltage hysteresis ΔE of 176.2 mV (Figure S12a) and a high Q_L/Q_H value of 2.44 (Figure S12b) are observed at 0.2 C, in agreement with the CV results (Figure 2a). In contrast, the CNTs−S/Gh-based battery exhibits smaller discharge/charge capacity, an increased voltage polarization (ΔE: 194.5 mV, Figure S12a) and a low Q_L/Q_H value (2.38, Figure S12b) in Figure 2c and Figure S11b. Lower polarization value ΔE and higher Q_L/Q_H value are indicative of the accelerated redox reaction kinetics and better catalysis of TPP for promoting conversion from short-chain LiPSs to Li_2S/Li_2S_2 in the Li−S battery. It is noteworthy that the CNTs−S/Gh/TPP-based battery produces a higher discharge capacity of 362.3 mAh g^{-1} than the CNTs−S/Gh-based battery (331.3 mAh g^{-1}) at the first plateau around 2.3 V (Figure 2d), which implies the higher active sulfur utilization rate and rapid liquid−liquid conversion.[29] Also, the CNTs−S/Gh/TPP-based battery shows a smaller interfacial energy barrier of 32.4 mV than that of CNTs−S/Gh-based battery (34.2 mV), indicating the promoted kinetics of Li_2S nucleation, deposition and conversion by the catalysis of TPP.[30]

Considering durability and high sulfur loading are critical parameters for the commercialization of Li−S batteries, the long-term cycle stabilities of the battery with CNTs−S/Gh/TPP electrode at sulfur loadings of ∼1.5 and 4.43 mg cm^{-2} were tested, respectively. From Figure 2e, after an activation treatment at 0.1 C for 10 cycles, the CNTs−S/Gh/TPP-based battery with a sulfur loading of ∼1.5 mg cm^{-2} at 1 C demonstrates a high discharge initial capacity of 842.7 mAh g^{-1} and a retained capacity of 455.6 mAh g^{-1} after 700 cycles as well as a high Coulombic efficiency of ∼98%, corresponding to a low degradation of 0.07% per cycle, showing its excellent inhibition ability of LiPS shuttling and kinetics enhancement. Under the same condition, the CNTs−S/Gh and CNTs−S electrodes can only deliver low initial discharge capacities of 642.5 and 545.7 mAh g^{-1} (Figure 2e and Figure S13), respectively. Their capacities rapidly decay to 330.1 (CNTs−S/Gh) and 240 mAh g^{-1} (CNTs−S) at the 500th cycle with higher degradations of 0.1% and 0.11% per cycle, due to the sluggish reaction kinetics of LiPSs and the irreversible sulfur loss. In Figure 2f, the thick CNTs−S/Gh/TPP electrode with a sulfur loading of 4.43 mg cm^{-2} retains an impressive discharge capacity of 551.5 mAh g^{-1} (capacity retention: 83.7%) and an areal capacity of 2.34 mAh cm^{-2} at 0.1 C after 180 cycles.

Mechanistic Insights into Catalytic Kinetics of Li−S Batteries. Apart from the strong anchoring effect by TPP, the catalysis of LiPS conversion is another vital factor for the outstanding electrochemical performance of the Li−S battery. To reveal the catalytic effectiveness and interfacial kinetics of TPP in improving the sulfur conversion reaction in Li−S batteries, the cathodes were analyzed by means of symmetric cells, galvanostatic intermittent titration technique (GITT), and electrochemical impedance spectroscopy (EIS). Li_2S_6 symmetric cells using CNTs/Gh/TPP and CNTs/Gh electrodes were assembled and measured with CV, respectively. Apparently, the CNTs/Gh/TPP-based cell harvests stronger redox currents than the CNTs/Gh-based cell (Figure 3a), implying that TPP provides access for electronic charge to reach electrode/LiPSs interface and trigger ultrafast LiPS conversion kinetics. Such accelerated charge transfer is further

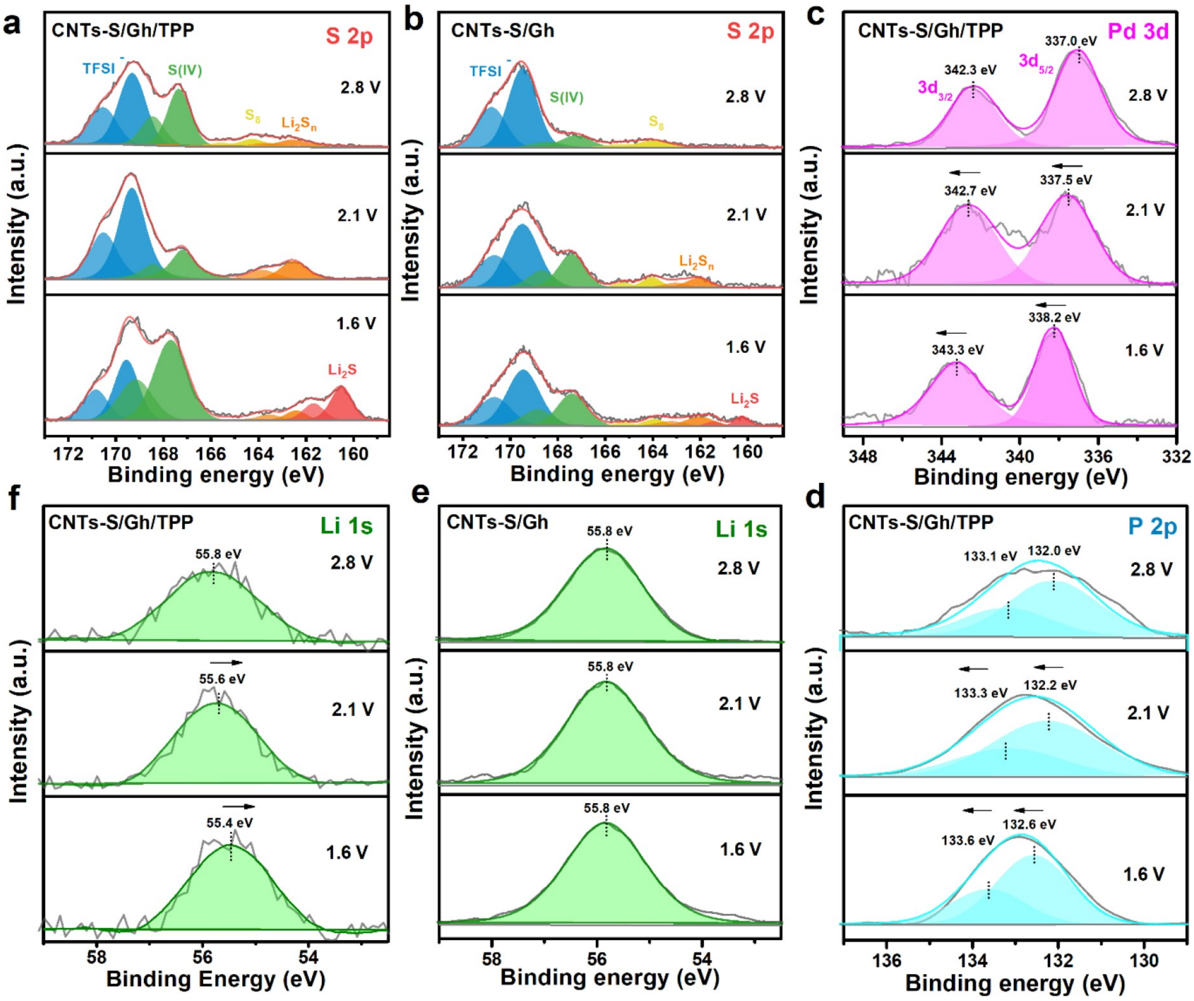

Figure 4. S 2p XPS spectra for (a) CNTs-S/Gh/TPP and (b) CNTs-S/Gh electrodes at different discharge states. The (c) Pd 3d and (d) P 2p XPS spectra for CNTs-S/Gh/TPP electrode at different discharge states. The Li 1s XPS spectra for (e) CNTs-S/Gh and (f) CNTs-S/Gh/TPP electrodes at different discharge states.

verified by EIS results (Figure 3b,c and Figure S14). From the Nyquist plots of two cells after different cycles and their corresponding analysis (Figure 3b and Figure S14), the cell with CNTs-S/Gh/TPP composite cathode exhibits lower charge transfer resistance (R_{ct}) and larger semi-infinite Warburg impedance with respect to the CNTs-S/Gh cathode, confirming the acceleration of electronic and ion transportation at the electrode and the improvement of the reaction kinetics toward LiPS conversion with assist of TPP.[31,32] Further important insights into the kinetically limiting processes are obtained by GITT.[33,34] In the experiments, a series of current pulses at 0.1 C are delivered, each pulse is followed by a relaxation period (2 h) to equilibrium. As shown in Figure 3d, the CNTs-S/Gh/TPP electrode presents a larger capacity of 1402.8 mAh g^{-1} than that of the CNTs-S/Gh electrode (1121.6 mAh g^{-1}). What's more, a smaller voltage change in CNTs-S/Gh/TPP electrode than that in CNTs-S/Gh sample is observed during charge/discharge progresses, suggesting a lower reaction resistance in CNTs-S/Gh/TPP electrode. It can be inferred that the CNTs-S/Gh/TPP electrode can enhance Li^+ insertion/extraction kinetics than CNTs-S/Gh sample.

In situ UV−vis spectroscopy is considered as an efficient tool to track the transformation of LiPS intermediates at the electrode/electrolyte interface during battery cycling.[35] Thus, CNTs/Gh/TPP and CNTs/Gh electrodes in Li_2S_8 solutions were detected by UV−vis spectroscopy at different discharge states, and the collected spectra are displayed in Figure S15. On the basis of our previous reports,[22,36] the absorbance peaks at 492, 475, 420, and 617 nm represent the species of S_8^{2-}, S_6^{2-}, S_4^{2-}, and S_3^{*-}, respectively.[37] In accordance with the relationship between the intensity and concentration, a further quantitative analysis of different LiPSs in Figure S15 was carried out by plotting the normalized peak intensity as a function of potential. Figure 3e−h compares the changes in normalized intensities of S_8^{2-}, S_6^{2-}, S_4^{2-}, and S_3^{*-} on the two electrodes during discharge. Unlike the CNTs/Gh electrode with much less intensity variation, the significant declines in the intensities of S_8^{2-}, S_6^{2-}, S_4^{2-}, and S_3^{*-} are observed on the TPP-containing electrode during the entire discharge process, indicating TPP has a vigorous converting function toward both long-chain and short-chain LiPSs.

For a more accurate demonstration of such a high LiPS conversion efficiency and mechanism, semi-in situ XPS measurements were conducted at CNTs-S/Gh/TPP and CNTs-S/Gh electrodes. The coin cell was discharged to different potential states at 0.2 C and then disassembled inside the glovebox to take out the separator and Li anode for

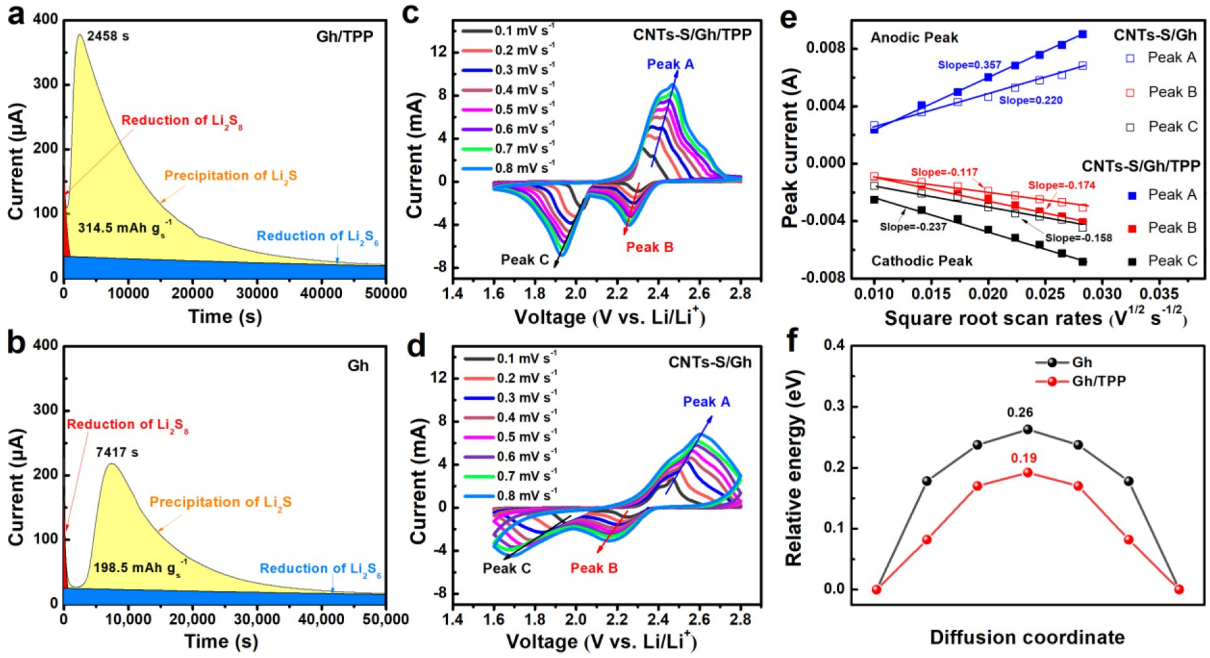

Figure 5. Potentiostatic discharge curves of Li_2S_8 solution on (a) Gh/TPP and (b) Gh electrodes at 2.05 V. CVs of (c) CNTs−S/Gh/TPP and (d) CNTs−S/Gh cathodes between 1.6 and 2.8 V at various scan rates. (e) Fitting lines of the peak currents in Figure 5c,d to square root scan rate. (f) Li^+ migration energy profiles on Gh/TPP and Gh surfaces.

photograph and extract the cathode for XPS analysis. The peaks between 166.0 and 172.0 eV are attributed to salt lithium bis(trifluoromethanesulfonyl)imide (LiTFSI, 169.5/170.6 eV) and sulfite arising from the decomposition of the LiTFSI (167.5/168.5 eV). For CNTs-S/Gh/TPP electrode, the S 2p XPS spectrum at 2.8 V shows main S_8 peaks (164.2/165.3 eV) with shoulder peaks of Li_2S_n (162.5/163.6 eV, $4 \leq n \leq 8$) in Figure 4a. Upon discharging to 2.1 V, the Li_2S_n ($4 \leq n \leq 8$) peaks become stronger. As the electrode is discharged to 1.6 V, the Li_2S peaks at lower binding energies of 160.5/161.7 eV dominate the spectrum with the weak Li_2S_n ($4 \leq n \leq 8$) peaks.[38] In contrast, the CNTs-S/Gh electrode shows lower signals for the sulfur species at different discharge states (Figure 4b), suggesting its lower conversion efficiency of LiPSs than the CNTs/Gh/TPP electrode. This can also be proved by the photographs of the separator and Li anode from the two cells after discharged to 1.6 V (Figure S16), where less yellow color and corrosion can be found on the separator and Li anode from CNTs-S/Gh/TPP-based cell, demonstrating that there are less LiPS shuttling and fast LiPS conversion in CNTs-S/Gh/TPP-based cell. Additionally, a significant shift in Pd 3d peaks toward higher binding energy is observed during discharging (Figure 4c), which can be ascribed to the electron transfer from Pd of TPP to S of LiPSs. Similarly, the P 2p peaks on CNTs/Gh/TPP electrode shift to higher binding energies (Figure 4d), while its Li 1s peak shifts from 55.8 eV to a lower binding energy of 55.4 eV (Figure 4f) during discharging from 2.8 to 1.6 V, demonstrating a strong binding and electron transfer between LiPS and TPP through P−Li bond. These findings are in consistent with the ex situ XPS and DFT results in Figure 1.

Given the liquid−solid conversion contributes nearly 75% of theoretical capacity during discharge, the acceleration effect in this important process should be carefully investigated. For the liquid−solid conversion kinetics, the Li_2S nucleation/deposition and Li^+ diffusion rate are usually significant parameters to guarantee fast electrochemical reaction in polysulfide transformation chemistry. Hence, the potentiostatic discharge experiments of Li_2S_8 solution were first designed on the surfaces of CNTs/Gh/TPP and CNTs/Gh. As shown in Figure 5a−b, three parts, corresponding to the reduction of Li_2S_8 (red), Li_2S_6 (blue), and the nucleation of solid Li_2S (yellow), respectively, contribute to the I−t curves.[39,40] It is evident that a potentiostatic current peak with a high nucleation capacity of 314.5 mAh g^{-1} for the CNTs/Gh/TPP composite cathode appears earlier than that for CNTs/Gh electrode (nucleation capacity: 198.5 mAh g^{-1}), revealing chemisorption and catalysis superiority of TPP toward accelerating the liquid−solid conversion kinetics and improving the utilization of active materials. After the Li_2S deposition, the Li_2S dissolution was also investigated by potentiostatically charging the cells at 2.35 V. As exhibited in Figure S17, a much earlier (1676 s) and a higher amount of Li_2S decomposition (corresponding to 285.3 mAh g^{-1}) on CNTs-S/Gh/TPP than the CNTs-S/Gh electrode (132.5 mAh g^{-1} at 2378 s) represent the best catalytical capability of TPP to enhance Li_2S oxidation kinetics. Besides, the Li^+ diffusion coefficient (D_{Li+}) can be quantitatively estimated based on the slope of the linear fitting line of peak current at various scan rates (Figure 5e) monitored by CVs (Figure 5c,d).[41,42] As presented in Table S3, the CNTs−S/Gh/TPP electrode exhibits the larger Li^+ diffusion coefficients for the cathodic and anodic peaks, further demonstrating that the usage of TPP in cathode is capable of boosting fast Li^+ transport and LiPS redox kinetics during discharge/charge processes. Meanwhile, climbing image nudged elastic band (CI-NEB) simulations were applied to calculate the migration barriers for Li^+ on anchoring materials. Figure S18 displays the front views of optimized atomic geometry conformations of Li^+ migration pathways on Gh/TPP and Gh surfaces. As shown in Figure 5f, the calculated energy barriers are 0.19 and 0.26 eV, corresponding to the surfaces of Gh/TPP and Gh, respectively, indicating the greater ability toward Li$^+$ mobilization and better reaction kinetics on Gh/TPP surface.

CONCLUSIONS

In summary, a TPP modified Gh interlayer has been successfully constructed in the cathode region of Li−S batteries. In the interlayer, the dissociation of a PPh_3 from the TPP catalyst reduces the steric hindrance for LiPSs and makes abundant sulfiphilic Pd sites exposed for absorbing/catalyzing LiPSs, while lithiophilic P atoms in the catalysts and the porous Gh conductive substrate ensure high-efficiency Li$^+$ and electron transmission. The synergistic function of the interlayer effectively retards the polysulfide shuttling and significantly enhances redox reaction kinetics, thus giving rise to a Li−S battery with outstanding electrochemical performance (capacity retention of 83.7% and areal capacity of 2.44 mAh cm^{-2} over 180 cycles at 0.1 C under a sulfur loading of 4.43 mg cm^{-2}). The present work provides a reasonable and new strategy for solving the shuttle effect and sluggish reaction kinetics problems in Li−S batteries.

ASSOCIATED CONTENT

Supporting Information

The Supporting Information is available free of charge at https://pubs.acs.org/doi/10.1021/acsaem.2c01078.

> Experimental section, including fabrication of CNTs-S cathodes with interlayers, material characterizations, cell assembly and electrochemical measurements, symmetric cell tests, visualized adsorption of LiPSs, Li_2S nucleation measurements, in situ UV−vis measurements, semi-in situ XPS, theoretical calculations; Schematic of the applications for Pd-based molecular catalysts; The P 2p and Pd 3d XPS spectra of Gh and Gh/TPP; FTIR spectra of Gh, TPP and Gh/TPP; BET adsorption−desorption curves and pore size distributions of Gh/TPP and Gh; The optimized local atomic structure and electron distribution between Li_2S_n (n = 8, 6, 4, 2, 1) species and Gh and Gh/TPP ($Pd(PPh_3)_x$, x = 3) surfaces predicted via DFT calculations; Optical photograph of TPP dissolved in DOL/DME solution; The rate performances of CNTs−S/Gh/TPP cathodes with different mass ratios of TPP to Gh; The CV curves of the CNTs−S/Gh/TPP and CNTs−S/Gh electrodes during the initial four cycles at a scan rate of 0.1 mV s^{-1}; The comparison of peak potentials for the CVs in Figure 2a; The Tafel slopes of the cathodic and anodic peaks in Figure 2a, corresponding to P_1, P_2 and P_3; The galvanostatic charge/discharge profiles of CNTs−S/Gh/TPP and CNTs−S/Gh electrodes at different rates for the second cycle; The comparisons of ΔE and Q_L/Q_H for the galvanostatic charge/discharge profiles at different rates in Figure S12; Cycling performance of CNTs−S electrode; The Nyquist plots of the two electrodes after 5 and 50 cycles; In situ UV−vis absorption spectra of CNTs/Gh/TPP and CNTs/Gh electrodes in Li_2S_8 solution during discharge; Optical photographs of the extracted Li anode and separator from the CNTs/Gh-based Li−S batteries after 50 cycles; Optical photographs of the extracted Li anode and separator from the CNTs/Gh/TPP-based Li−S batteries after 50 cycles; Potentiostatic charge curves of Li_2S_8 solution on Gh and Gh/TPP electrodes at 2.35 V; Side views of Li$^+$ migration routes on Gh/TPP ($Pd(PPh_3)_x$, x = 3) and Gh; Energies for a TPP molecule to dissociate different PPh_3; The voltage hysteresis (ΔV) and collection coefficient (I_L/I_H) values derived from the CV data in Figure 2a; The D_{Li^+} values of CNTs-S/Gh/TPP and CNTs-S/Gh cathodes at different peaks (PDF)

AUTHOR INFORMATION

Corresponding Authors

Shuo Yang − *Key Laboratory of Carbon Materials of Zhejiang Province, Wenzhou University, Wenzhou 325035, P. R. China; College of Electrical and Electronic Engineering, Wenzhou University, Wenzhou 325035, P. R. China;* orcid.org/0000-0001-8906-5289; Email: yangshuo@wzu.edu.cn

Zhi Yang − *Key Laboratory of Carbon Materials of Zhejiang Province, Wenzhou University, Wenzhou 325035, P. R. China;* orcid.org/0000-0002-9265-5041; Email: yang201079@126.com

Authors

Binbin Gu − *Key Laboratory of Carbon Materials of Zhejiang Province, Wenzhou University, Wenzhou 325035, P. R. China*

Dong Cai − *Key Laboratory of Carbon Materials of Zhejiang Province, Wenzhou University, Wenzhou 325035, P. R. China*

Yangyang Dong − *Key Laboratory of Carbon Materials of Zhejiang Province, Wenzhou University, Wenzhou 325035, P. R. China*

Shuang Yu − *Key Laboratory of Carbon Materials of Zhejiang Province, Wenzhou University, Wenzhou 325035, P. R. China*

Tingting Li − *Key Laboratory of Carbon Materials of Zhejiang Province, Wenzhou University, Wenzhou 325035, P. R. China*

Huagui Nie − *Key Laboratory of Carbon Materials of Zhejiang Province, Wenzhou University, Wenzhou 325035, P. R. China*

Complete contact information is available at: https://pubs.acs.org/10.1021/acsaem.2c01078

Notes

The authors declare no competing financial interest.

ACKNOWLEDGMENTS

This research was funded in part by National Natural Science Foundation of China (Grant Nos. 22109119, 51972238, 22105147, and 21875166), Natural Science Foundation of Zhejiang Province (Grant Nos. LQ19B030006, LR18E020001, and LQ22B030003), Major Scientific and Technological Innovation Project of Wenzhou City (Grant No. ZG2021013), and Basic Scientific Research Projects of Wenzhou City (Grant Nos. G2020002 and H20210006).

REFERENCES

(1) Yang, Y.; Zheng, G.; Cui, Y. Nanostructured Sulfur Cathodes. *Chem. Soc. Rev.* **2013**, *42*, 3018−3032.

(2) Li, Z.; Zhang, J. T.; Chen, Y. M.; Li, J.; Lou, X. W. Pie-like Electrode Design for High-Energy Density Lithium-Sulfur Batteries. *Nat. Commun.* **2015**, *6*, 8850.

(3) Ji, X.; Lee, K. T.; Nazar, L. F. A Highly Ordered Nanostructured Carbon-Sulphur Cathode for Lithium-Sulphur Batteries. *Nat. Mater.* **2009**, *8*, 500−506.

(4) Zhou, G.; Zhao, Y.; Manthiram, A. Dual-Confined Flexible Sulfur Cathodes Encapsulated in Nitrogen-Doped Double-Shelled Hollow Carbon Spheres and Wrapped with Graphene for Li-S Batteries. *Adv. Energy Mater.* **2015**, *5*, 1402263.

(5) Cheng, X.-B.; Huang, J.-Q.; Zhang, Q.; Peng, H.-J.; Zhao, M.-Q.; Wei, F. Aligned Carbon Nanotube/Sulfur Composite Cathodes with High Sulfur Content for Lithium-Sulfur Batteries. *Nano Energy* **2014**, *4*, 65−72.

(6) Zhou, G.; Paek, E.; Hwang, G. S.; Manthiram, A. Long-Life Li/Polysulphide Batteries with High Sulphur Loading Enabled by Lightweight Three-Dimensional Nitrogen/Sulphur-Codoped Graphene Sponge. *Nat. Commun.* **2015**, *6*, 7760.

(7) Su, Y.-S.; Manthiram, A. Lithium-Sulphur Batteries with a Microporous Carbon Paper as a Bifunctional Interlayer. *Nat. Commun.* **2012**, *3*, 1166.

(8) Wang, Z.; Dong, Y.; Li, H.; Zhao, Z.; Wu, H. B.; Hao, C.; Liu, S.; Qiu, J.; Lou, X. W. Enhancing Lithium-Sulphur Battery Performance by Strongly Binding the Discharge Products on Amino-Functionalized Reduced Graphene Oxide. *Nat. Commun.* **2014**, *5*, 5002.

(9) Zhou, T.; Lv, W.; Li, J.; Zhou, G.; Zhao, Y.; Fan, S.; Liu, B.; Li, B.; Kang, F.; Yang, Q.-H. Twinborn TiO_2-TiN Heterostructures Enabling Smooth Trapping-Diffusion-Conversion of Polysulfides towards Ultralong Life Lithium-Sulfur Batteries. *Energy Environ. Sci.* **2017**, *10*, 1694−1703.

(10) Kong, W.; Yan, L.; Luo, Y.; Wang, D.; Jiang, K.; Li, Q.; Fan, S.; Wang, J. Ultrathin MnO_2/Graphene Oxide/Carbon Nanotube Interlayer as Efficient Polysulfide-Trapping Shield for High-Performance Li-S Batteries. *Adv. Funct. Mater.* **2017**, *27*, 1606663.

(11) Zhang, Z.; Wu, G.; Ji, H.; Chen, D.; Xia, D.; Gao, K.; Xu, J.; Mao, B.; Yi, S.; Zhang, L.; Wang, Y.; Zhou, Y.; Kang, L.; Gao, Y. 2D/1D V_2O_5 Nanoplates Anchored Carbon Nanofibers as Efficient Separator Interlayer for Highly Stable Lithium-Sulfur Battery. *Nanomaterials* **2020**, *10*, 705.

(12) Demir-Cakan, R.; Morcrette, M.; Nouar, F.; Davoisne, C.; Devic, T.; Gonbeau, D.; Dominko, R.; Serre, C.; Férey, G.; Tarascon, J.-M. Cathode Composites for Li-S Batteries via the Use of Oxygenated Porous Architectures. *J. Am. Chem. Soc.* **2011**, *133*, 16154−16160.

(13) Liang, X.; Rangom, Y.; Kwok, C. Y.; Pang, Q.; Nazar, L. F. Interwoven MXene Nanosheet/Carbon-Nanotube Composites as Li-S Cathode Hosts. *Adv. Mater.* **2017**, *29*, 1603040.

(14) Liang, X.; Garsuch, A.; Nazar, L. F. Sulfur Cathodes Based on Conductive MXene Nanosheets for High-Performance Lithium-Sulfur Batteries. *Angew. Chem., Int. Ed.* **2015**, *127*, 3979−3983.

(15) Cheng, Z.; Xiao, Z.; Pan, H.; Wang, S.; Wang, R. Elastic Sandwich-Type rGO-VS_2/S Composites with High Tap Density: Structural and Chemical Cooperativity Enabling Lithium-Sulfur Batteries with High Energy Density. *Adv. Energy Mater.* **2018**, *8*, 1702337.

(16) Zhong, Y.; Yin, L.; He, P.; Liu, W.; Wu, Z.; Wang, H. Surface Chemistry in Cobalt Phosphide-Stabilized Lithium-Sulfur Batteries. *J. Am. Chem. Soc.* **2018**, *140*, 1455−1459.

(17) Mi, Y.; Liu, W.; Li, X.; Zhuang, J.; Zhou, H.; Wang, H. High-Performance Li-S Battery Cathode with Catalyst-Like Carbon Nanotube-MoP Promoting Polysulfide Redox. *Nano Res.* **2017**, *10*, 3698−3705.

(18) Beletskaya, I. P.; Cheprakov, A. V. The Heck Reaction as a Sharpening Stone of Palladium Catalysis. *Chem. Rev.* **2000**, *100*, 3009−3066.

(19) Lyons, T. W.; Sanford, M. S. Palladium-Catalyzed Ligand-Directed C-H Functionalization Reactions. *Chem. Rev.* **2010**, *110*, 1147−1169.

(20) Zhu, Z.; Yin, H.; Wang, Y.; Chuang, C.-H.; Xing, L.; Dong, M.; Lu, Y.-R.; Casillas-Garcia, G.; Zheng, Y.; Chen, S.; Dou, Y.; Liu, P.; Cheng, Q.; Zhao, H. Coexisting Single-Atomic Fe and Ni Sites on Hierarchically Ordered Porous Carbon as a Highly Efficient ORR Electrocatalyst. *Adv. Mater.* **2020**, *32*, 2004670.

(21) Dong, Y.; Cai, D.; Li, T.; Yang, S.; Zhou, X.; Ge, Y.; Tang, H.; Nie, H.; Yang, Z. Sulfur Reduction Catalyst Design Inspired by Elemental Periodic Expansion Concept for Lithium-Sulfur Batteries. *ACS Nano* **2022**, *16*, 6414−6425.

(22) Ding, X.; Yang, S.; Zhou, S.; Zhan, Y.; Lai, Y.; Zhou, X.; Xu, X.; Nie, H.; Huang, S.; Yang, Z. Biomimetic Molecule Catalysts to Promote the Conversion of Polysulfides for Advanced Lithium-Sulfur Batteries. *Adv. Funct. Mater.* **2020**, *30*, 2003354.

(23) Zhang, J.; Shi, Y.; Ding, Y.; Peng, L.; Zhang, W.; Yu, G. A Conductive Molecular Framework Derived Li_2S/N,P-Codoped Carbon Cathode for Advanced Lithium-Sulfur Batteries. *Adv. Energy Mater.* **2017**, *7*, 1602876.

(24) Peng, H.-J.; Zhang, Z.-W.; Huang, J.-Q.; Zhang, G.; Xie, J.; Xu, W.-T.; Shi, J.-L.; Chen, X.; Cheng, X.-B.; Zhang, Q. A Cooperative Interface for Highly Efficient Lithium-Sulfur Batteries. *Adv. Mater.* **2016**, *28*, 9551−9558.

(25) Hua, W.; Yang, Z.; Nie, H.; Li, Z.; Yang, J.; Guo, Z.; Ruan, C.; Chen, X.; Huang, S. Polysulfide-Scission Reagents for the Suppression of the Shuttle Effect in Lithium-Sulfur Batteries. *ACS Nano* **2017**, *11*, 2209−2218.

(26) Rehman, S.; Guo, S.; Hou, Y. Rational Design of Si/SiO_2@ Hierarchical Porous Carbon Spheres as Efficient Polysulfide Reservoirs for High-Performance Li-S Battery. *Adv. Mater.* **2016**, *28*, 3167−3172.

(27) Xiao, Z.; Yang, Z.; Wang, L.; Nie, H.; Zhong, M.; Lai, Q.; Xu, X.; Zhang, L.; Huang, S. A Lightweight TiO_2/Graphene Interlayer, Applied as a Highly Effective Polysulfide Absorbent for Fast, Long-Life Lithium-Sulfur Batteries. *Adv. Mater.* **2015**, *27*, 2891−2898.

(28) Wang, L.; Yang, Z.; Nie, H.; Gu, C.; Hua, W.; Xu, X.; Chen, X.; Chen, Y.; Huang, S. A Lightweight Multifunctional Interlayer of Sulfur-Nitrogen Dual-Doped Graphene for Ultrafast, Long-Life Lithium-Sulfur Batteries. *J. Mater. Chem. A* **2016**, *4*, 15343−15352.

(29) Wu, Z.; Chen, S.; Wang, L.; Deng, Q.; Zeng, Z.; Wang, J.; Deng, S. Implanting Nickel and Cobalt Phosphide into Well-Defined Carbon Nanocages: A Synergistic Adsorption-Electrocatalysis Separator Mediator for Durable High-Power Li-S Batteries. *Energy Storage Mater.* **2021**, *38*, 381−388.

(30) Yang, X.; Gao, X.; Sun, Q.; Jand, S. P.; Yu, Y.; Zhao, Y.; Li, X.; Adair, K.; Kuo, L.-Y.; Rohrer, J.; Liang, J.; Lin, X.; Banis, M. N.; Hu, Y.; Zhang, H.; Li, X.; Li, R.; Zhang, H.; Kaghazchi, P.; Sham, T.-K.; Sun, X. Promoting the Transformation of Li_2S_2 to Li_2S: Significantly Increasing Utilization of Active Materials for High-Sulfur-Loading Li-S Batteries. *Adv. Mater.* **2019**, *31*, 1901220.

(31) Peng, H.-J.; Hou, T.-Z.; Zhang, Q.; Huang, J.-Q.; Cheng, X.-B.; Guo, M.-Q.; Yuan, Z.; He, L.-Y.; Wei, F. Strongly Coupled Interfaces between a Heterogeneous Carbon Host and a Sulfur-Containing Guest for Highly Stable Lithium-Sulfur Batteries: Mechanistic Insight into Capacity Degradation. *Adv. Mater. Interfaces* **2014**, *1*, 1400227.

(32) Iskandar, F.; Setiawan, B.; Mayangsari, T. R.; Maharsi, R.; Purwanto, A.; Aimon, A. H. Electrochemical Impedance Analysis of Polyvinylpyrrolidone-Coated Sulfur/Reduced Graphene Oxide (S/rGO) Electrode. *Mater. Res. Express* **2019**, *6*, 025514.

(33) Dibden, J. W.; Meddings, N.; Owen, J. R.; Garcia-Araez, N. Quantitative GITT Analysis of a Model System with Applications to Lithium-Sulfur Batteries. *ChemElectroChem.* **2018**, *5*, 445−454.

(34) Zha, C.; Zhu, X.; Deng, J.; Zhou, Y.; Li, Y.; Chen, J.; Ding, P.; Hu, Y.; Li, Y.; Chen, H. Facet-Tailoring Five-Coordinated Ti Sites and Structure-Optimizing Electron Transfer in a Bifunctional Cathode with Titanium Nitride Nanowire Array to Boost the Performance of Li_2S_6-Based Lithium-Sulfur Batteries. *Energy Storage Mater.* **2020**, *26*, 40−45.

(35) Xu, N.; Qian, T.; Liu, X.; Liu, J.; Chen, Y.; Yan, C. Greatly Suppressed Shuttle Effect for Improved Lithium Sulfur Battery Performance through Short Chain Intermediates. *Nano Lett.* **2017**, *17*, 538−543.

(36) Zhang, Y.; Yang, S.; Zhou, S.; Zhang, L.; Gu, B.; Dong, Y.; Kong, S.; Cai, D.; Fang, G.; Nie, H.; Yang, Z. Oxygen Doping in

Antimony Sulfide Nanosheets to Facilitate Catalytic Conversion of Polysulfides for Lithium-Sulfur Batteries. *Chem. Commun.* **2021**, *57*, 3255−3258.

(37) Kim, B.-S.; Park, S.-M. In Situ Spectroelectrochemical Studies on the Reduction of Sulfur in Dimethyl Sulfoxide Solutions. *J. Electrochem. Soc.* **1993**, *140*, 115−122.

(38) Liu, Z.; He, X.; Fang, C.; Camacho-Forero, L. E.; Zhao, Y.; Fu, Y.; Feng, J.; Kostecki, R.; Balbuena, P. B.; Zhang, J.; Lei, J.; Liu, G. Reversible Crosslinked Polymer Binder for Recyclable Lithium Sulfur Batteries with High Performance. *Adv. Funct. Mater.* **2020**, *30*, 2003605.

(39) Fan, F. Y.; Carter, W. C.; Chiang, Y.-M. Mechanism and Kinetics of Li_2S Precipitation in Lithium-Sulfur Batteries. *Adv. Mater.* **2015**, *27*, 5203−5209.

(40) Li, Z.; Zhou, Y.; Wang, Y.; Lu, Y.-C. Solvent-Mediated Li_2S Electrodeposition: A Critical Manipulator in Lithium-Sulfur Batteries. *Adv. Energy Mater.* **2019**, *9*, 1802207.

(41) Zhou, G.; Tian, H.; Jin, Y.; Tao, X.; Liu, B.; Zhang, R.; Seh, Z. W.; Zhuo, D.; Liu, Y.; Sun, J.; Zhao, J.; Zu, C.; Wu, D. S.; Zhang, Q.; Cui, Y. Catalytic Oxidation of Li_2S on the Surface of Metal Sulfides for Li-S Batteries. *Proc. Natl. Acad. Sci. U. S. A.* **2017**, *114*, 840−845.

(42) Tao, X.; Wang, J.; Liu, C.; Wang, H.; Yao, H.; Zheng, G.; Seh, Z. W.; Cai, Q.; Li, W.; Zhou, G.; Zu, C.; Cui, Y. Balancing Surface Adsorption and Diffusion of Lithium-Polysulfides on Nonconductive Oxides for Lithium-Sulfur Battery Design. *Nat. Commun.* **2016**, *7*, 11203.

https://doi.org/10.1021/acsaem.2c01078
ACS Appl. Energy Mater. 2022, 5, 8538−8546